Influence (Ce and Sm) co-doping ZnO nanorods on the structural, optical and electrical properties of the fabricated Schottky diode using chemical bath deposition

Mustafa A. Ahmed[a,b], Liza Coetsee[c], Walter E. Meyer[a], Jackie M. Nel[a]

[a]*Physics Department, University of Pretoria, Private Bag X20, 0028, Hatfield, South Africa*
[b]*Physics Department, Faculty of Education, University of Khartoum, P.O Box 321, Omdurman, Sudan*
[c]*Physics Department, University of the Free State, P. O Box 339, 9300, Bloemfontein, South Africa*

Abstract

Schottky diodes based on ZnO nanorods, undoped and co-doped with different concentrations (0.0, 0.2, 0.4, 0.6 and 0.8 at.%) of Ce and Sm, were fabricated on glass and on n-Si (111) substrates using chemical bath deposition assisted with the sol-gel spin coating. The ZnO maintained its hexagonal shape up to higher levels of doping (0.8 at.%) with the growth rate being suppressed by Ce and Sm co-doping. The as-synthesized nanorods were found to be highly crystalline and no impurities or peaks related to Ce and Sm or their oxides were observed. Room temperature Raman spectroscopy revealed that the prominent E_2 high peak shifted towards a lower wave number and the intensity decreased upon doping. X-ray photoelectron spectroscopy studies at room temperature showed that the presence of Zn and O in all samples with small amounts of Ce and Sm being detected at doping levels of 0.8 at.%. Photoluminescence studies at room temperature revealed a weak ultraviolet emission and a strong deep level (visible) emission. Deconvolution of the visible emission spectra showed that more than one defect contributed to the visible emission. The *I-V* characteristics of the fabricated Schottky diode devices measured at room temperature showed that the Ce and Sm co-doping increased the generation-recombination process in the fabricated Schottky diodes. Furthermore, the current transport mechanism in the fabricated Schottky devices at a lower voltage (0.0 to ~ 0.6 V) was dominated by ohmic conduction mechanism, while at voltages greater than 0.6 V, the space charge limited current and the trap filled limit voltage mechanism dominated.

Keywords: ZnO; Chemical bath deposition; Structural properties; Optical properties; Electrical properties.

1. Introduction

In the last few decades, nanomaterials such as nanowires, nanotubes and nanorods have been the subject of many studies due to their potential use in a wide range of devices such as transistors, photodiodes, sensing application and Schottky diode devices. The physical, chemical and optical properties of these nanomaterials can significantly vary from their bulk counterpart due to the large surface area to volume ratio [1]. Metal oxide semiconductor nanomaterials have found interest from many researchers owing to their chemical, sensing, photo-detection and piezoelectric properties [2]. Among these oxides, ZnO has attracted much attention and has been studied extensively due to its excellent optical, optoelectronic, electrical, gas-sensing, and photochemical properties. Synthesis and characterization of one dimensional (1D) semiconductor materials have recently attracted more interest due to their physical properties that enable them to play a major role in optoelectronic and nanoscale electronic devices [3, 4, 5, 6, 7]. ZnO has a band gap of 3.37 eV and large exciton energy of 60 meV at room temperature. This properties make it a promising material with photonic properties in UV or blue spectral window [8]. The chemical and physical properties of ZnO can be altered by doping with different elements. Due to it is wide band gap, ZnO can be used as a host lattice for doping with different cations. Rare earth (RE) ions are often used in different host materials as an activator because

Email address: mustafa.sonbl@gmail.com (Mustafa A. Ahmed)

of their high fluorescence efficiencies and narrow line fluorescence bands as well as their electrical properties. There is also a potential active layer in the visible emission due to the large gap of ZnO. RE doped ZnO semiconductor has attracted much attention to the scientific community due to its optical properties that is dependent on the particle size [9]. It is well known that doping ZnO with RE ions can generate traps for photo-generated charge carries and decrease the generation-recombination (electron-hole) rate [10]. Moreover, excitation of RE ions is accompanied with energy transfer from the host semiconductor to the RE ions [11]. Many reports on RE elements doping ZnO are available for example Sm [10, 12], Eu [13, 14, 15], Yb, Er, La [16, 17] and Ce [18, 19, 20, 21, 22]. Among the RE ions, Ce doping has attracted much attention because of it is unique properties: for examples (1) the redox couple Ce^{3+}/Ce^{4+} that allows the oxidized cerium to shift between CeO_2 and Ce_2O_3 under oxidizing condition, (2) control over modifying the morphological properties of the host and (3) easy formation of oxygen vacancies [18]. Sm ions were also used as dopants for ZnO due their optical and electrical properties. Tsuji *et al.* [11] found sharp emission lines from intra $4f$ transition in Sm^{3+} at room temperature using an excitation wavelength above the energy bandgap of ZnO. Recently, ZnO nanostructures have been used extensively as Schottky diode devices [23, 24, 25]. Mehmet Yilmaz [26] fabricated a Schottky diode based on Co doping ZnO thin films on a p-type Si substrate. He found that the ideality factor of the fabricated Schottky diode decreased with increasing the Co contents. Yilmaz *et al.* [27] also fabricated a Schottky diode devices based on ZnO thin films doped with F using spray pyrolysis. In their study they found that the ideality factor decreased with increasing the F contents while the barrier height increased upon increasing the F concentrations.

Growth of ZnO nanostructures can be achieved by using techniques such as metal organic chemical vapour deposition [28], vapour-liquid-solid [5], thermal evaporation [29], radio-frequency magnetron sputtering [30], pulsed laser deposition [31], spray pyrolysis [32, 26, 27] and epitaxial electrodeposition [33]. These techniques have been used successfully to obtain highly oriented ZnO nanorods. However, many of these require specific conditions for successful reaction, such as high temperature and pressure which result in preventing the large-scale production of this material. On the other hand, chemical solution processes greatly facilitated the fabrication of well-aligned ZnO nanorods on a large scale at relatively low temperature. Herein, the low temperature chemical bath deposition assisted with sol-gel spin coating technique were adapted in this study.

In our previous results reported in [34, 35] both Sm and Ce have shown to be a good candidate as a Schottky diode when doped with ZnO nanorods fabricated on an indium tin oxide substrate. These nanorods have exhibited a good optical and electrical properties. We believe that doping of ZnO nanorods with Ce and Sm together will have an effect on the structural, optical and electrical (i.e. diode characteristic) properties. To the best of our knowledge, there are only a few reports a available on the effect that doping ZnO nanorods, with RE metals, has on the properties of Schottky diode devices. None of theses reports, however, reported or investigated specially the effect of Ce and Sm co-doped ZnO nanorods on the Schottky diode properties. In this study, we therefore report on the effect that co-doping ZnO nanorods with Ce and Sm has on the structural, optical and electrical properties of Schottky diode devices. Ce and Sm co-doped ZnO nanorods exhibited well crystalline samples with a good PL properties. The fabricated Schottky diode showed a modification of the transport mechanism in the diode due to the co-doping effect.

2. EXPERIMENT

2.1. Materials

The following precursors were used as received: zinc acetate dihydrate (Merck, 98.0%), zinc nitrate hexahydrate (Sigma Aldrich, 98.0%), samarium nitrate hexahydrate (Sigma Aldrich, 99.9%), cerium nitrate hexahydrate (Sigma Aldrich,99.999%), hexamethylenetetramine (HMTA) (Sigma Aldrich, 98.0%), propan-2-ol (Merck, 99.95%) and mono-ethanolamine (MEA) (Merck, 98%). Before the growth of aligned ZnO nanorods, a deposition of the ZnO seed layer is required. Prior to the ZnO seed layer deposition, glass and Si (111) substrates were cleaned using a procedure described in our previous work [36, 37].

2.2. Deposition of the seed layer

A Zinc oxide seed layer solution was prepared by dissolving zinc acetate dihydrate (0.5M) in a mixture of MEA and propan-2-ol (60 ml). The molar ratio between zinc acetate and MEA was kept at 1.0. The solution was then stirred for 2 hr at 550 rpm and at 60 °C until a clear and transparent solution was obtained. Thereafter, the solution was aged

for 72 hrs before using it, to increase the viscosity. The aged solution was then spin coated on cleaned substrates (glass and Si) at 3000 rpm for 30 seconds until desired thickness were obtained (60 - 80) nm. After each coating, substrates with films deposited were dried at 150 °C for 5 min in an oven in air, and the films were finally annealed at 150 °C for 15 min before growing the nanorods.

2.3. Growth of the nanorods

For the fabrication of the ZnO nanorods, zinc nitrate hexahydrate (0.1 M) and HMTA (0.1 M) were separately dissolved in deionised water under continuous stirring for 15 min and finally mixed together. The resulting milky solution was then placed in a hot water bath preheated at 90 °C. Seeded substrates were then immersed and positioned in such a way that the seeded side faced downward. For the Ce and Sm co-doped ZnO nanorods' fabrication, samarium and cerium nitrate hexahydrate with a concentration ($Zn_{1-x-y}Ce_xSm_yO$, $x + y = 0.0$, 0.2, 0.4, 0.6 and 0.8 at.%, x : y = 1 : 1) were separately dissolved in deionised water and stirred for 15 min. After that, Ce and Sm solutions were added to the mixture of zinc nitrate, HMTA and mixed throughly. The procedure that was used for the ZnO nanorods was then followed. The depositions for all samples were done in an open beaker for 2 hrs. Finally, the substrates with deposited nanorods were rinsed several times with deionised water to remove the residuals and it was blown dry with nitrogen gas. It should be mentioned that for all doped and undoped samples the seeded ZnO thin films were undoped.

2.4. Fabrication of the ohmic and Schottky contacts

AuSb alloy (200 nm thick and area of 2.5 cm^2) was evaporated resistively on the backside (unpolished side) of the Si substrate (ρ is 1.4 - 1.8 Ω.cm and carrier concentrations of 2.26×10^{15} cm^{-3}) and then annealed in nitrogen atmosphere at 460 °C for 3 min. For the Schottky contacts, a circular Pd contact (thickness of 100 nm and $\approx 3.0\times10^{-3}$ cm^2) was evaporated resistively on top of the nanorods using a mechanical shadow mask. The deposition rate and initial pressure in the chamber were 0.1 nm/s and 2.5×10^{-6} mbar, respectively. Thus, A Pd/ZnO/n-Si/AuSb Schottky diode based on undoped and Ce, Sm co-doped ZnO nanorods, were fabricated.

3. CHARACTERIZATION

The as-synthesized nanorods were characterized in terms of their structure and surface morphology using a Rigaku SmartLab X-ray diffractometer (λ = 1.54059 nm) and a Zeiss crossbeam 540 field emission scanning electron microscope (540 FEG-SEM), respectively. X-ray photoelectron spectroscopy (XPS) data were acquired at room temperature with a PHI 5000 scanning ESCA Microprobe. A 100 μm diameter monochromatic Al$K\alpha$ x-ray beam with $h\nu$ = 1486.6 eV was used to analyze the different binding energies. A low energy Ar^+ ion gun and neutralizer electron gun were used to minimize the surface charging. The overall energy resolution for all spectra was set to 0.5 eV. Multipack software version 9.0 was used to analyze the spectra and to identify their electronic state using Gaussian-Lorentz fit. Raman spectroscopy measurements were acquired at room temperature in the 200 - 800 nm range , with high-resolution confocal Raman imaging (WITec alpha 300R confocal Raman microscope, λ = 532 nm). Photoluminescence (PL) spectroscopy of all samples were studied at room temperature using He-Cd laser in the 350 - 850 nm range, with excitation wavelength λ = 325 nm. Finally, the electrical measurements on the fabricated Schottky diode based on undoped and (Ce, Sm) co-doped ZnO nanorods were studied at room temperature using a SMU (key sight B2912A) Keithley 230 meter.

4. RESULTS AND DISCUSSIONS

4.1. Structural and morphological results

Figure. 1(A) shows the XRD patterns of the as-synthesized undoped and (Ce, Sm) co-doped ZnO nanorods at different doping concentrations, measured at room temperature. The presented peaks in the XRD patterns are indexed to the hexagonal wurtzite ZnO structure. It can be seen for all samples that the nanorods have preferred orientation along the (002) plane, which indicate that the nanorods were grown perpendicular to the substrates. No other peaks related to Ce and Sm or their oxides were observed in the spectrum, which implies that the dopants have substituted the Zn^{+2} and incorporated successfully into the ZnO lattice. It was noted that the position of (002) peak fluctuated to higher and lower 2θ values after doping as can be see in Fig. 1(B). The fluctuation of the peak position could be due

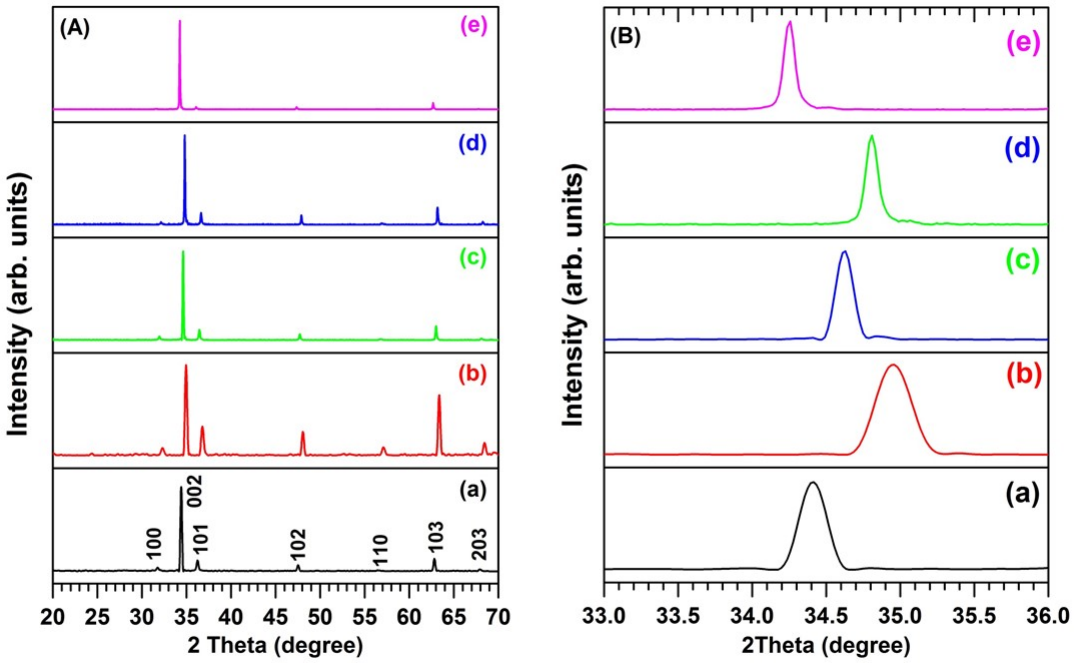

Figure 1: (A) Room temperature XRD patterns: (a) pure, (b) 0.2, (c) 0.4, (d) 0.6 and (e) is 0.8 at.% Ce and Sm co-doping ZnO nanorods. (B) An enlargement of the (002) peak area.

to the replacement of the Zn^{+2} (0.74 Å) with a larger ionic radius of Ce^{+3} (1.03 Å) and Sm^{+3} (0.92 Å). The full width at half maximum (FWHM) was also found to increase first and then decreased with increasing doping concentrations implying that the dopants have improved the crystallinity. Furthermore, the presence of a prominent, sharp and more intense peak along the (002) plane confirmed the improvement of the crystalline quality.

The crystallographic properties of the as-grown pure ZnO and the (Ce, Sm) co-doping ZnO nanorods calculated as described previously [34] are presented in Table. 1. The lattice parameters for undoped ZnO nanorods were found to be in good agreement with the JCPDS card number 36 - 1451. We observed that, the lattice parameters fluctuated with increasing the dopant concentrations, indicating that the lattice constants were affected by the co-doping with Ce and Sm due to the larger ionic radius of Ce and Sm compared to Zn. The lattice parameters first decreased at a doping concentrations of 0.2 at.%, then increased at 0.4 at.% before decreasing again at 0.6 at.%. At the higher concentrations of 0.8 at.% the lattice parameters increased again. Similar results were previously reported for Sm doped ZnO nanoparticles [38]. The average crystallite size (D) calculated from XRD data using Scherrer's formula was found to increase with increasing the Ce and Sm concentrations (see Table. 1). The increase in the crystallite size can be attributed to the distortion of the lattice owing to the substitution of Zn^{+2} ions with Sm^{+3} and Ce^{+3} ions. Moreover, the volume of the unit cell of the as-synthesized samples calculated as previously described [38] was found to be in the range of 46.11 - 52.34 $Å^3$. Furthermore, the length of the ZnO nanorods decreased with increasing the dopant content, emphasizing that the Ce and Sm suppressed the nanorod growth.

Figure 2((a) - (e)) shows the SEM images of as-synthesised undoped and (Ce, Sm) co-doped ZnO nanorods at different concentration levels (0.0, 0.2, 0.4, 0.6 and 0.8 at.%). As can be seen, ZnO nanorods maintain their hexagonal structure up to a doping percentage of 0.8 at.%. The measured lengths were found to be in the range of 1.5 μm - 980 nm, while the diameter raged between 150 - 340 nm, (increasing with increasing dopant concentrations).

4.2. X-ray photoelectrons spectroscopy

Figure 3(A) shows the room temperature survey scan of undoped and (Ce, Sm) co-doped ZnO nanorods measured in the range 0 - 1400 eV. The main peaks in the survey scan were assigned to the Zn, O, C, Ce and Sm and the binding

Table 1: Lattice parameters, peak position, FWHM, crystallite size, volume of the unit cell obtained from XRD, nanorod length obtained from SEM studies and oxygen peak positions obtained from XPS studies.

at.%	Lattice parameter(nm)		2θ	FWHM	Crystallite size	Volume	length	Oxygen position (eV)		
	a	c	(degree)	(degree)	μm	Å	nm	O_1	O_2	O_3
0.0	0.3249	0.5206	34.41	0.219	40	47.59	1.5	530.2	531.5	532.5
0.2	0.3195	0.5128	34.95	0.288	30	52.34	1.5	530	531.2	532
0.4	0.3229	0.5176	34.62	0.143	61	46.73	1.2	529.9	531.3	532.1
0.6	0.3216	0.5148	34.81	0.124	70	46.11	1.1	529.8	530.9	531.8
0.8	0.3262	0.5230	34.25	0.082	106	48.19	1.0	530.1	531.2	532.1

energies were calibrated by using the C 1s peak at 284.5 eV. Figure 3(B) shows the high resolution spectra of the Zn 2p core level for the undoped and (Ce, Sm) co-doped ZnO nanorods. The line shape of the Zn 2p core level for the undoped ZnO (Fig. 3(B-(a))) revealed a doublet, Zn $2p_{3/2}$ and Zn $2p_{1/2}$ located at the binding energy 1021.4 and 1044.2 eV, respectively, and they were ascribed to the Zn in the ZnO [39, 40]. The spin orbital splitting for undoped ZnO was found to be 22.8 eV which is in good agreement within the standard value of ZnO [41]. For the Ce and Sm co-doped ZnO samples at 0.2, 0.4, 0.6 and 0.8 at.%, the spin orbital splitting were found to be 23.0, 23.1, 23,1, and 23.2, respectively. These values are slightly higher than that of undoped ZnO which could be due to the effect of doping. The binding energy differences calculated from XPS indicated that the Zn atoms are in the +2 oxidation state.

Figure 4 shows the deconvoluted O 1s spectra for the as-synthesized undoped and co-doped ZnO nanorods using a Gaussian distribution. The O 1s for all samples showed three different peak. The position of these binding energies were tabulated in Table 1. The lower binding energy component labeled ($\mathbf{O}_1$) centered at around 530 nm was attributed to the O^{-2} ions in the ZnO lattice [42]. The area of this binding energy peak determines how much oxygen is associated with Zn-O. Interestingly, the intensity of this peak was found to decrease with increasing the doping concentration. This indicates that the Ce and Sm dopants replaced the Zn ions in the ZnO lattice structure. The medium binding energy component labeled ($\mathbf{O}_2$) centered around 531 nm was ascribed to O^{-2} oxygen deficiency within the ZnO matrix in the Zn-OH group [42]. Finally, the higher binding energy component labeled ($\mathbf{O}_3$) centered around 532 was attributed to the chemisorbed oxygen such as CO_2, H_2O and oxygen vacancies that increase with increasing the dopant concentration [43].

4.3. Raman Spectroscopy

Raman spectroscopy is known as a non-destructive tool that can be used to study the vibrational mode and phase purity and it is very sensitive to the microstructure of materials such as thin films, nanorods and nanotubes etc. The room temperature Raman spectra for the undoped ZnO and Ce and Sm co-doped ZnO nanorods in the 200 - 800 cm^{-1} wave number range, excited by the 514.15 nm line of an argon laser is shown in Fig. 5. All peaks in Raman spectra are assigned to the wurtzite ZnO crystal structure [34, 44]. From Raman spectra only two vibrational modes were observed namely: E_2 (high) and A_1 located at 435.50 cm^{-1} and 560 cm^{-1}, respectively. The E_2 (high) mode is known as the characteristic peak of the hexagonal wurtzite ZnO and has been previously reported for ZnO nanorods [34]. No other peaks related to impurities, Ce and/or Sm and their oxides were observed by Raman spectroscopy. The E_2 (high) appeared as a prominent peak that indicated the as-synthesised samples were crystalline. It was also found that the intensity of the E_2 (high) mode decreased with increasing the dopant concentration, except for the sample doped at 0.4 at.%, in which the intensity increased. Moreover, the position of the E_2 (high) mode shifted towards a lower wavenumber with increasing doping levels compared to the undoped ZnO nanorods. The shift in the peak position and the decrease in the peak's intensity could be attributed to the doping effect and incorporation of the dopants into the ZnO lattice. This increase in the peak intensity in the case of 0.4 at.% doping could be attributed to the improvements in the crystalline quality [45]. Furthermore, the A_1 vibration mode has been previously reported and ascribed to the oxygen vacancy defects or zinc interstitial, and also to an increase in the carrier concentrations [46, 47, 48]. The Raman spectroscopy results support the XRD results presented above and the oxygen deficiency related to the XPS results.

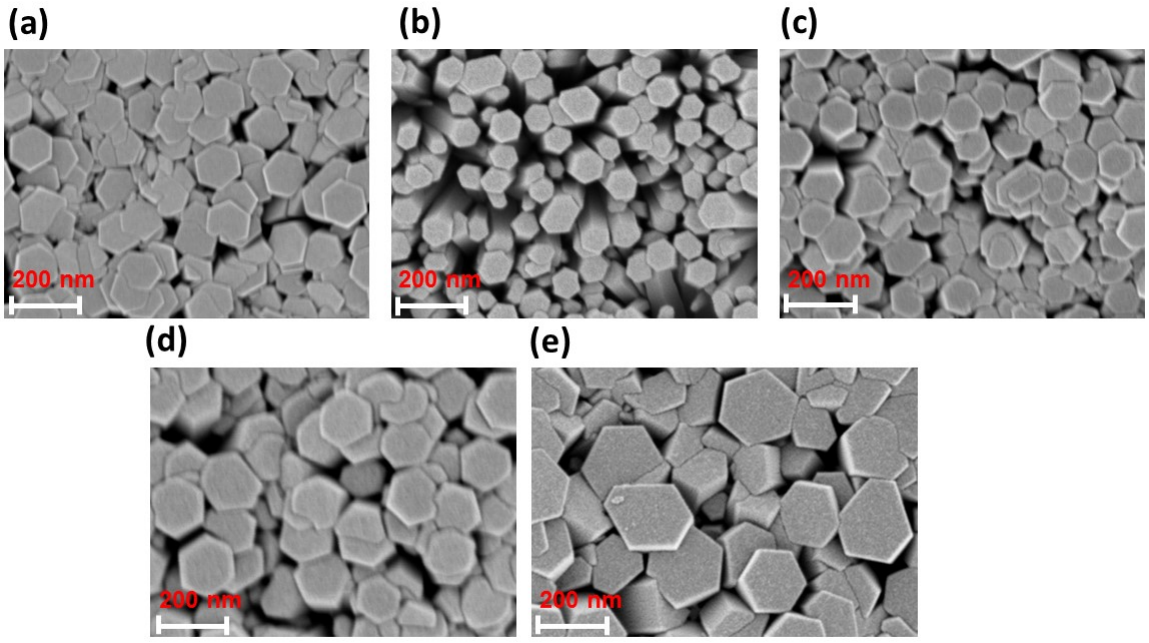

Figure 2: SEM images of the undoped ZnO and Ce and Sm co-doped ZnO nanorods at different concentrations levels of doping: (a) 0.0, (b) 0.2, (c) 0.4, (d) 0.6 and (e) is 0.8 at.%.

4.4. Photoluminescence spectroscopy

Room temperature PL spectra of undoped and (Ce, Sm) co-doped ZnO nanorods in the 350 - 850 nm range is shown in Fig. 6. Normally, ZnO has two distinct emissions, excitonic emission (band to band) located in the UV region around 378 nm and the deep level emission in the visible light region [49, 50]. The excitonic emission presented in Fig. 6(B) can be understood by the free exciton recombinations (i.e. electrons and holes combination) through exciton-exciton collision. As evidenced in Fig. 6(A), the UV peak emission for all samples located at 376 nm is weak compared to the visible light emission, which is similar to the PL spectra reported by Kumar and co-workers [50]. It has been reported that the presence of $Zn(OH)_2$ at the surface could be a reason for the weak UV and strong visible emission [51]. V Kumar *et al.* [52] also reported similar behaviour for ZnO prepared by combustion method. It is noted from Fig. 6(B) that the UV emission increased with 0.2 at.% Ce and Sm doping concentration and then it decreased with further increase in doping concentration.

It has been observed from Fig. 6(A) that, all samples showed a strong deep level emission peak in the 450 to 850 nm range. The maximum emission was obtained with pure ZnO nanorods sample. Generally, ZnO exhibits a deep level emission band that is ascribed to an intrinsic defect that depends on the fabrication process, such as oxygen vacancies, zinc vacancies, zinc interstitial and oxygen interstitials [53, 54]. In our case, the procedure that we used to fabricate the nanorods can easily result in defects being formed apart from the doping that can also introduce defects. After doping, the emission centre first blue-shifted at 0.2 at.% and then it red-shifted with further increase in doping concentration as demonstrated in Fig.6(A). Interestingly, the intensity of the doped samples first decreased with an increase in the doping concentration up to 0.4 at.% and it increased with a further increase in the doping concentration, see Fig. 6(A). To identify the multiple emission bands that contributed to the broad visible emission of all samples, de-convolution of the spectrum were carried out using Gaussian fits. The results of the de-convoluted spectra for all samples are shown in Fig. 7. As we can see, the de-convoluted spectra for the undoped ZnO nanorods and for the sample doped at 0.8 at.% showed three defects related to the visible emission bands; however, for the rest of the samples four defects were observed. The positions of these emission bands are presented in Table 2. The bands in

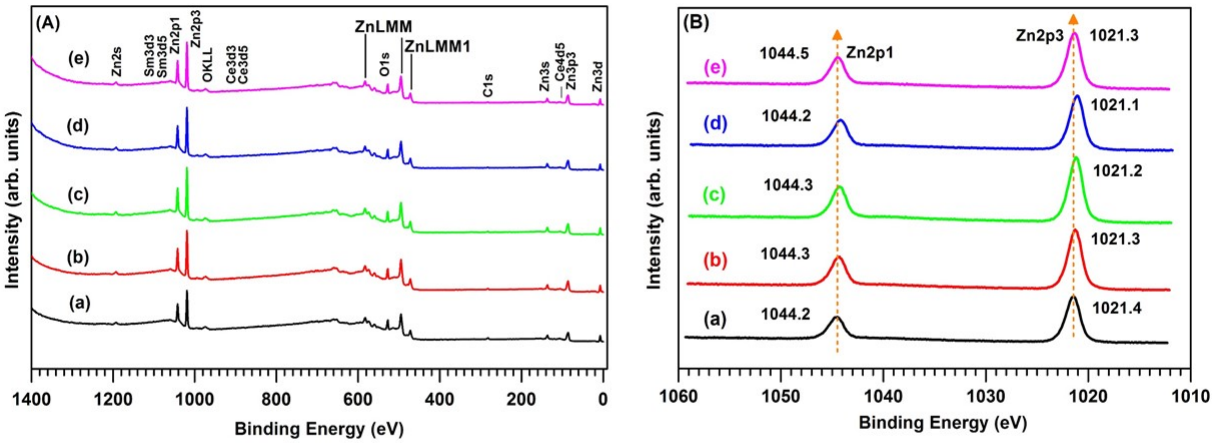

Figure 3: (A) XPS survey spectra of the undoped ZnO and Ce and Sm co-doped ZnO nanorods with different levels of concentrations: (a) 0.0, (b) 0.2, (c) 0.4, (d) 0.6 and (e) is 0.8 at.%.

the 522 - 555 nm range (green emission) may be due to the transition of electrons from zinc interstitials to oxygen interstitials or from the conduction band to singly ionized oxygen vacancies [55, 56]. Bands at 577 and 589 nm were attributed to oxygen interstitials [56, 57]. Finally, the bands that were in the orange-red emission range (i.e. 612 - 753 nm) were due to the oxygen vacancies and interstitials [50, 57]. The presence of oxygen vacancies were confirmed by the XPS results described earlier. It can therefore be concluded from the PL results that more than one defect contributed to the visible emission.

Table 2: Peak positions of the de-convoluted visible emission spectra of undoped ZnO and (Ce, Sm) co-doped ZnO nanorods using a Gaussian function.

Ce, Sm concentration	Emission center (nm)	Peak1 (nm)	Peak2 (nm)	Peak3 (nm)	Peak4 (nm)
0.0	591	549	612	675	- -
0.2	575	533	589	645	753
0.4	592	522	577	654	732
0.6	589	538	589	641	638
0.8	595	555	622	675	742

4.5. Electrical characterization

4.5.1. I-V characteristics

Figure 8(A) shows the *I-V* characteristics of the Pd/ZnO/n-Si/AuSb Schottky diodes based on undoped and (Ce, Sm) co-doped ZnO nanorods at the different levels of doping measured at room temperature. It must be stated that

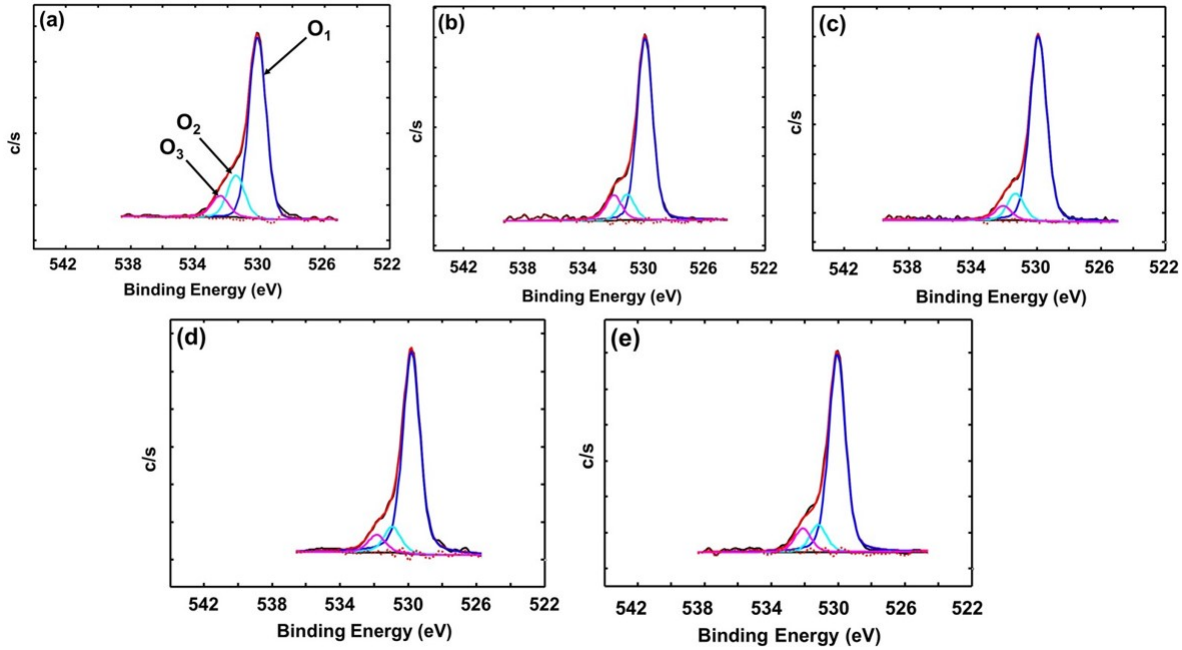

Figure 4: O 1s high resolution XPS spectra of undoped ZnO, Ce and Sm co-doped ZnO nanorods with different levels of doping: (a) 0.0, (b) 0.2, (c) 0.4, (d) 0.6 and (e) is 0.8 at.%.

the fabricated Schottky diode devices based on undoped and co-doped with Ce and Sm have been fabricated on three Si substrates, and that the *I-V* characteristics from these devices were all similar and no significant differences were observed. It must also be mentioned that when using Au as Schottky contact no rectification was observed on any of the samples. The as-synthesized samples showed rectification behaviour with the maximum rectification ratio obtained with the undoped ZnO nanorods. The behaviour of the Pd/ZnO/n-Si/AuSb Schottky diodes in the forward bias can be analyzed using the thermionic emission theory [58]:

$$I = I_s \left[\exp 1 - \left(\frac{-q(V - IR_s)}{k_\beta T} \right) \right] \tag{1}$$

where, q is the electronic charge, V is the applied voltage, R_s is the series resistance and I_s is the saturation current which is given by:

$$I_s = SA^*T^2 \left[-q \frac{\Phi_{B_0}}{nk_\beta T} \right] \tag{2}$$

where, S is the diode contact area, A^* is the effective Richardson constant (32 $\mathrm{Acm^{-2}K^{-2}}$), Φ_{B_0} represents the zero bias Schottky barrier height, k_β is the Boltzmann constant, T is the absolute temperature and n is the diode ideality factor, $n = 1$ for an ideal diode. The obtained n, Φ_{B_0} and the I_s values from the linear fit are summarized in Table 3. The nanorods in the undoped and co-doped ZnO, underneath the Pd contact, could be considered as a summation of individuals Schottky contacts aligned together in parallel. It can be observed from Fig. 8 that the rectification order decreased upon introducing the dopant. The leakage currents for the doped samples were higher compared to the undoped ZnO by approximately an order of magnitudes. The obtained n values for all sample were higher than the value of the ideal Schottky diodes, and were found to increase with increasing the amounts of Ce and Sm up to 0.4 at.%. The value however decreased for higher concentrations. The deviation of the ideality factor from the unity could be attributed to some factors, for example, series resistance, surface and interface states, the voltage drop across

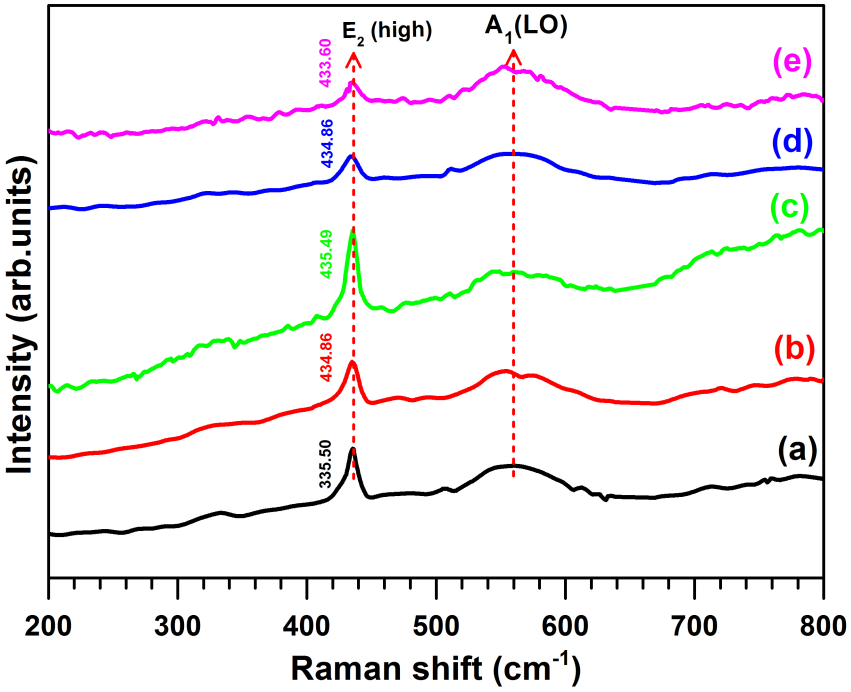

Figure 5: (Color online) Raman spectra of undoped ZnO, Ce and Sm co-doped ZnO nanorods: (a) 0.0, (b) 0.2, (c) 0.4, (d) 0.6 and (e) is 0.8 at.%.

the metal-semiconductor junction, interfacial dielectric layers between metal and semiconductor [59, 60], and/or the presence of inhomogeneities in the barrier heights [61, 62]. It has been reported that the interface states are introduced due to factors such as oxidation of semiconductor surfaces caused by air exposure and the chemical reaction during the growth process [63, 64]. Moreover, the presence of higher values of n indicating that the transport mechanism is controlled by more than mechanisms and the thermionic emission theory is no longer dominated.

The Schottky barrier height for all samples deviated from the theoretical value (calculated from the difference between the work function of the Pd Schottky contact (5.22 eV) and the ZnO electron affinity (4.20 eV). Φ_{B_0} was found to decrease with increasing the Ce and Sm concentrations [65]. Generally, the deviation of Φ_{B_0} from the theoretical value is attributed to inhomogeneities in the barrier height at the interface resulting in a deviation from the linearity of *I-V* and also the interface states [61]. Moreover, the presence of various defects (discussed in the PL section above) might also be responsible for this deviation [63]. Interestingly, in the range between 0.0 to 0.6 eV, all samples showed a plateau region which is less pronounced in the case of the undoped ZnO, and it becomes more pronounced after doping, especially at higher concentrations (0.8 at.%), see Fig. 8(A). This plateau is typically due to the generation-recombination between the electrons and holes [61]. Furthermore, the leakage current was found to increase with increasing doping concentration, which is attributed to the large density of interface states caused by the defects, and these interface states are distributed continuously within the energy gap. It can be seen from Fig. 8(A) in the forward bias that the current transport mechanism in fabricated devices composed of two mechanisms.

4.5.2. Energy band gap diagram

Figure 9 shows the energy band gap diagram of Pd/n-ZnO/n-Si/AuSb at the thermal equilibrium according to Anderson model [66]. According to this model, the interface states is assumed to be neglected and the Fermi level in ZnO lies just below the conduction band edge. As shown in Fig. 9, the position of the Fermi energy in the bulk Si substrate was calculated to be 0.22 eV below the conduction band edge of the Si. The band offset in the conduction

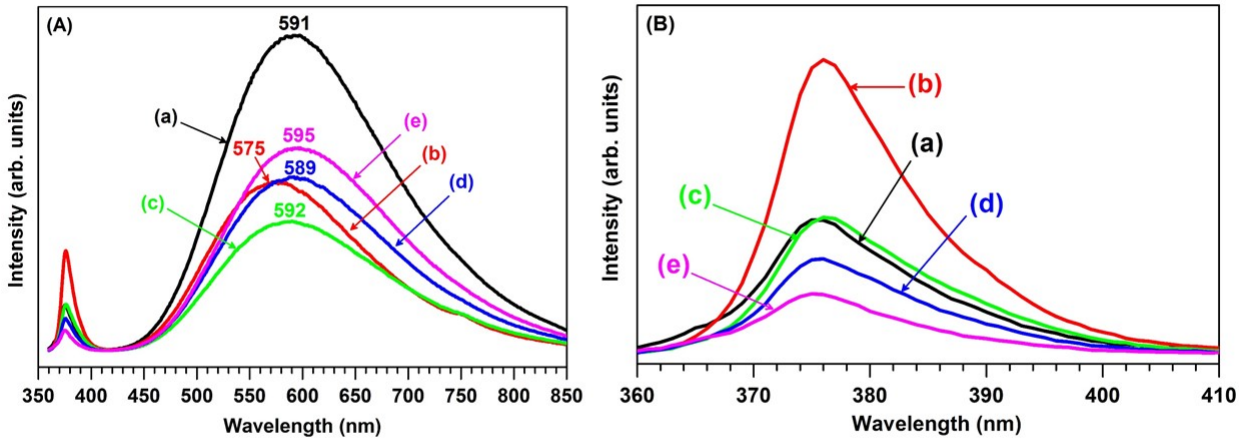

Figure 6: (A) PL spectra of undoped, Sm and Ce co-doped ZnO nanorods at different levels of doping measured at room temperature: (a) pure, (b) 0.2, (c) 0.4, (d) 0.6 and (e) is 0.8 at.% Ce and Sm co-doping ZnO nanorods. (B) An enlargement of the UV emission peaks.

band (ΔE_c) and the valence bad (ΔE_v) were determined using the following equations

$$\Delta E_c = \chi_{ZnO} - \chi_{Si} \tag{3}$$

$$\Delta E_v = (E_{g_{ZnO}} - E_{g_{Si}}) - \Delta E_c \tag{4}$$

where χ_{ZnO}, χ_{Si}, are the electron affinity of ZnO and Si, respectively. Energy gap of ZnO nanorods and bulk Si are respectively denoted by $E_{g_{ZnO}}$ and $E_{g_{Si}}$. The band gap of undoped ZnO nanorods and co-doped with Ce and Sm at 0.0, 0.2, 0.4, 0.6 and 0.8 at.% were obtained from Tauc's plots (not shown here) and found to be 3.25, 3.27, 3.24, 3.25 and 3.27 eV, respectively. By using the electron affinity of ZnO (4.35 eV) and Si (4.05) the value of ΔE_c calculated using Equation 3 is 0.3 eV which is the energy barrier height seeing by the majority electrons carriers to overcome from Si to n-ZnO. The values of ΔE_v for undoped ZnO nanorods, Ce and Sm co-doped ZnO nanorods were calculated using Equation 4 and the values were tabulated in Table 3. In the presence of interface states or defects within the semiconductor band gap, which is unavoidable in the method used to fabricate the diode devices (i.e. chemical bath deposition) the Fermi energy is no longer within the conduction band and is rather pinned by interface states [61]. This pining of the Fermi energy level will makes the energy barrier height to be independent of the semiconductor work function. The pining of the Fermi energy level is about 1/3 of the band gap [61]. Therefore, the change in the energy barrier height will affect the charge transport mechanism through the Schottky diode devices.

4.5.3. Current transport mechanisms

To study the transport phenomena of the fabricated Schottky diodes based on undoped and (Ce, Sm) co-doped ZnO nanorods, a logarithmic plot of the *I-V* characteristic is shown in Fig. 8(B). Figure 8(B) shows two distinct regions, implying different transport mechanisms for each region. The presence of deep traps at the interface would

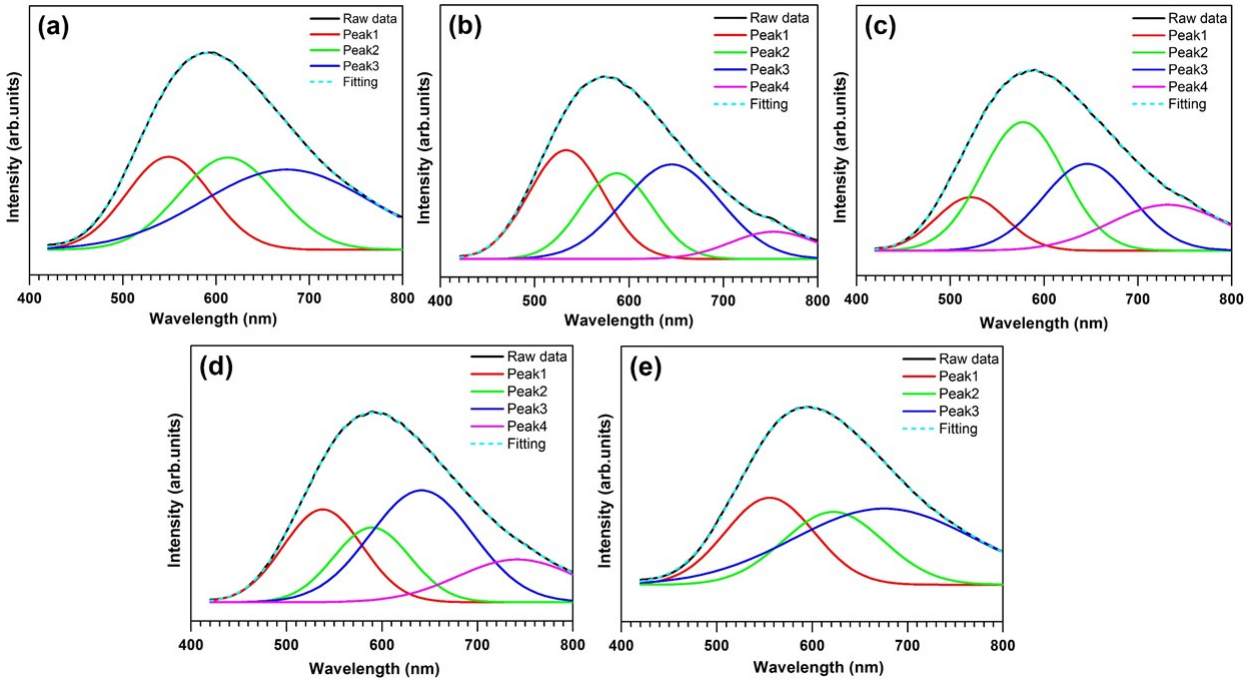

Figure 7: (Color online) De-convolution of PL visible spectra of undoped ZnO, Ce and Sm co-doped ZnO nanorods using Gaussian function: (a) 0.0, (b) 0.2, (c) 0.4, (d) 0.6 and (e) is 0.8 at.%.

modify the charge transport and therefore affect the slope of the *I-V* characteristic. As can be seen in Fig. 8(B) (region *I*) that, for all samples and at low voltages (0.0 - $\sim$ 0.6 eV) the current was linearly dependent on the voltage (i.e. $I \sim V$). The slope in this region for all samples is around unity, indicating that the transport mechanism dominated by an ohmic conduction mechanism, although, in this region, due to the low voltage, the injection of the carrier from the electrode to a semiconductor was reduced. In region *II* the current transport mechanism followed an exponential relation (i.e. $I \propto \exp(cV)$). The slope of this region for undoped and (Ce, Sm) co-doped ZnO nanorods at different levels of doping, namely 0.0, 0.2, 0.4, 0.6 and 0.8 at.% were found to be 10.0, 11.0, 6.3, 10.4 and 10.0, respectively, implying that the transport mechanism in this region were dominated by the trap filled limit voltage (V_{TFL}) and space charge-limited current (SCLC) mechanisms. The V_{TFL} is defined as the voltage at which the traps are filled with carries. As the applied voltage to the junction increases the injected charge carriers also increased resulting in traps filled with carries [67]. The SCLC transport mechanism is controlled by the presence of traps within the forbidden gap of ZnO nanorods. The SCLC occurs when the concentration of the equilibrium charge is negligible compared to the injected one, and as a result, a space charge region near the injecting electrodes will be formed [68].

5. Conclusion

Schottky diodes based on undoped and (Ce, Sm) co-doped ZnO nanorods were successfully fabricated on an a n-Si substrate using chemical bath deposition assisted with sol-gel spin coating technique. FESEM images revealed that the ZnO has maintained its hexagonal structure up to higher levels of doping. XRD results revealed that the as-synthesized nanorods were highly crystalline with preferential growth along the c-axis, as expected. No other impurities related to Ce and Sm or their oxides were seen in the XRD spectra indicating that Ce and Sm have successfully been incorporated into the ZnO lattice. Raman spectroscopy measurements at room temperature showed that the prominent E_2 high peak shifted toward a lower wavenumber and that the intensity decreased after doping. The XPS results showed the expected spectra associated with Zn and O, and at higher doping concentrations (0.8 at.%) the presence of Ce and Sm

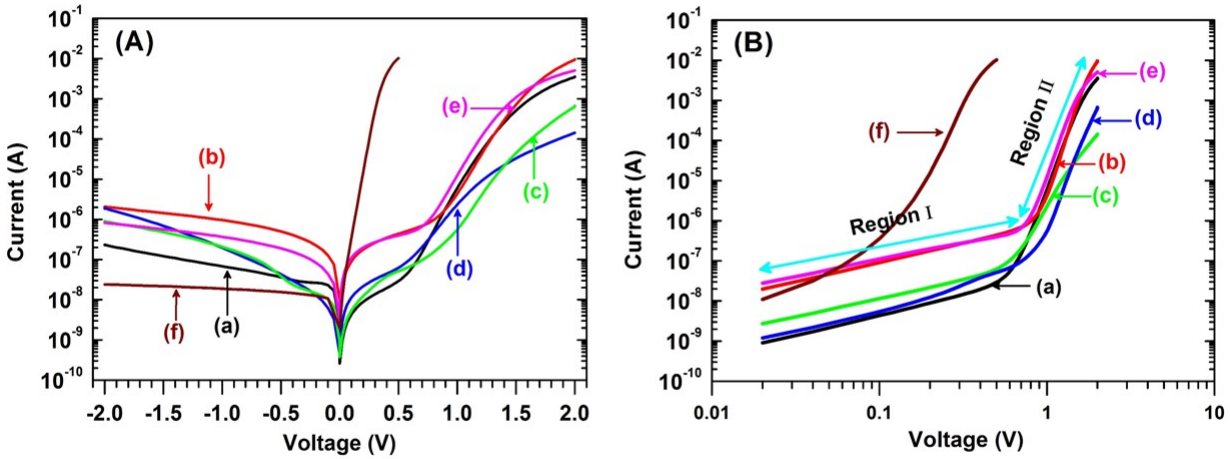

Figure 8: (Color online) (A) The *I-V* characteristics and (B) the transport mechanism of undoped, Ce and Sm co-doped ZnO nanorods at different levels of doping: (a) 0.0, (b) 0.2, (c) 0.4, (d) 0.6 and (e) is 0.8 at.%. (f) Represent the *I-V* characteristics of Pd-n-Si/AuSb Schottky diodes.

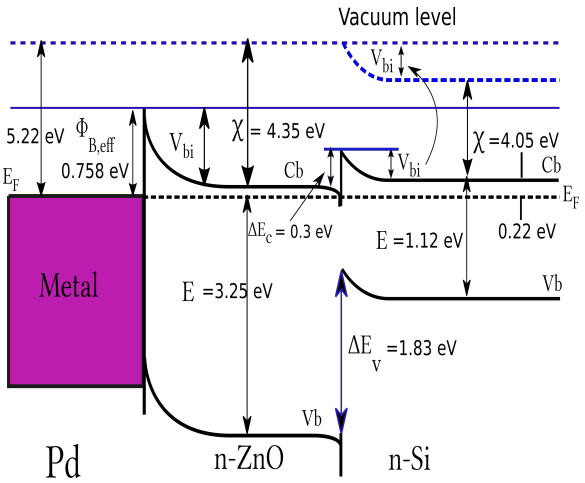

Figure 9: Energy band gap diagram of Pd/n-ZnO/n-Si/AuSb, by neglecting the density of interface state.

were detected. The analysis of high-resolution spectra revealed the presence of oxygen vacancies for both undoped and (Ce, Sm) co-doped ZnO nanorods. Room temperature PL spectra showed a weak UV emission peak and strong deep level emission. The intensity of the deep level emission first decreased upon doping, up to 0.4 at.%, and then enhanced again at higher concentrations. The deconvolution of the deep level emission spectra revealed that more than one defect contributed to the visible emission. The *I-V* characteristics of the fabricated Schottky diode devices based on undoped and (Ce, Sm) co-doped ZnO nanorods at room temperature revealed a rectification behaviour.

Table 3: Schottky diodes parameters extracted from *I-V* characteristics, ideality factor (n), Schottky barrier height (Φ_B), series resistance (R_s), saturation current (I_s) and conduction band offset (ΔE_v)

Ce and Sm at.%	n	Φ_B (eV)	R_s Ω	I_s (A)	ΔE_v (eV)
0.0	3.32	0.784	103.22	44.51×10^{-12}	1.83
0.2	3.88	0.745	25.82	206.28×10^{-12}	1.58
0.4	5.11	0.704	2.17 k	1.03×10^{-9}	1.81
0.6	4.57	0.758	215.64	122.00×10^{-12}	1.83
0.8	3.70	0.734	95.32	315.38×10^{-12}	1.85
n-Si	1.06	0.750	11.79	8.24×10^{-9}	−−

The ideality factor decreased with increasing doping concentrations. The *I-V* characteristics also revealed that Ce and Sm co-doping of ZnO nanorods had increased the generation-recombination process in the device. Furthermore, the current transport mechanism at lower voltages (up to ~ 0.6 V) was dominated by the ohmic conduction transport mechanism and at the higher voltage (above ~ 0.6 V), the SCLC and the V_{TFL} were the dominant transport mechanism.

Acknowledgment

This work is supported by the South African Research Foundation (NRF) grant no: 91550 and 111744. The opinions, findings and conclusion are those of the authors and the NRF accepts no responsibility whatsoever in this regard. The authors would like to thanks Prof. Hendrik Swart, from the department Physics at the University of Free State for XRD, UV-vis and PL measurements.

References

[1] E. Elssfah, C. Tang, From $Al_4B_2O_9$ nanowires to $Al_{11}B_4O_{33}$: Eu nanowires, J. Phys. Chem. C 111 (23) (2007) 8176–8179.

[2] J. G. Lu, P. Chang, Z. Fan, Quasi-one-dimensional metal oxide materialssynthesis, properties and applications, Mater. Sci. Eng. R Rep. 52 (1) (2006) 49–91.

[3] J. Hu, T. W. Odom, C. M. Lieber, Chemistry and physics in one dimension: synthesis and properties of nanowires and nanotubes, Acc. Chemi. Res. 32 (5) (1999) 435–445.

[4] Y. Cui, C. M. Lieber, Functional nanoscale electronic devices assembled using silicon nanowire building blocks, Science 291 (5505) (2001) 851–853.

[5] P. Yang, H. Yan, S. Mao, R. Russo, J. Johnson, R. Saykally, N. Morris, J. Pham, R. He, H. Choi, et al., Controlled growth of ZnO nanowires and their optical properties, Adv. Funct. Mater. 12 (5) (2002) 323–331.

[6] Z. Dai, Z. W. Pan, Z. L. Wang, Novel nanostructures of functional oxides synthesized by thermal evaporation, Adv. Funct. Mater. 13 (1) (2003) 9–24.

[7] T. H. Lee, H. J. Sue, X. Cheng, ZnO and conjugated polymer bulk heterojunction solar cells containing ZnO nanorod photoanode, Nanotechnology 22 (28) (2011) 285401.

[8] P. Zhang, W. Liu, ZnO QD/@ PMAA-co-PDMAEMA nonviral vector for plasmid DNA delivery and bioimaging, Biomaterials 31 (11) (2010) 3087–3094.

[9] M. Khatamian, A. Khandar, B. Divband, M. Haghighi, S. Ebrahimiasl, Heterogeneous photocatalytic degradation of 4-nitrophenol in aqueous suspension by Ln (La^{3+}, Nd^{3+} or Sm^{3+}) doped ZnO nanoparticles, J. Mol. Cata. A Chem. 365 (2012) 120–127.

[10] J. Sin, S. Lam, K. Lee, A. R. Mohamed, Preparation and photocatalytic properties of visible light-driven samarium-doped ZnO nanorods, Ceram. Int. 39 (5) (2013) 5833–5843.

[11] T. Tsuji, Y. Terai, M. hakim, M. Kawabata, Y. Fujiwara, Photoluminescence properties of Sm-doped ZnO grown by sputtering-assisted metalorganic chemical vapor deposition, J. Non-Cryst. Solids 358 (17) (2012) 2443–2445.

[12] P. Velusamy, R. R. Babu, K. Aparna, Effect of Sm doping on the physical properties of ZnO thin films deposited by spray pyrolysis technique, in: AIP Conf. Proceed., Vol. 1832, AIP Publishing, 2017, p. 080085.

[13] O. Lupan, T. Pauporte, B. Viana, P. Aschehoug, M. Ahmadi, B. R. Cuenya, Y. Rudzevich, Y. Lin, L. Chow, Eu-doped ZnO nanowire arrays grown by electrodeposition, Appl. Surf. Sci. 282 (2013) 782–788.

[14] P. Korake, A. Kadam, K. Garadkar, Photocatalytic activity of Eu^{3+}-doped ZnO nanorods synthesized via microwave assisted technique, J. Rare Earths 32 (4) (2014) 306–313.

[15] M. Najafi, H. Haratizadeh, M. Ghezellou, The effect of annealing, synthesis temperature and structure on photoluminescence properties of Eu-doped ZnO nanorods, J. Nanostruct. 5 (2) (2015) 129–135.

[16] M. Balestrieri, G. Ferblantier, S. Colis, G. Schmerber, C. Ulhaq-Bouillet, D. Muller, A. Slaoui, A. Dinia, Structural and optical properties of Yb-doped ZnO films deposited by magnetron reactive sputtering for photon conversion, Sol. Energy Mater. Sol. Cells 117 (2013) 363–371.

[17] R. Zamiri, A. Lemos, A. Reblo, H. A. Ahangar, J. Ferreira, Effects of rare-earth (Er, La and Yb) doping on morphology and structure properties of ZnO nanostructures prepared by wet chemical method, Ceram. Int. 40 (1) (2014) 523–529.
[18] A. J. Kulandaisamy, V. Elavalagan, P. Shankar, G. K. Mani, K. J. Babu, J. B. B. Rayappan, Nanostructured Cerium-doped ZnO thin film–A breath sensor, Ceram. Int. 42 (16) (2016) 18289–18295.
[19] J. Lang, J. Wang, Q. Zhang, X. Li, Q. Han, M. Wei, Y. Sui, D. Wang, J. Yang, Chemical precipitation synthesis and significant enhancement in photocatalytic activity of Ce-doped ZnO nanoparticles, Ceram. Int. 42 (12) (2016) 14175–14181.
[20] A. Chelouche, T. Touam, M. Tazerout, D. Djouadi, F. Boudjouan, Effect of Li codoping on highly oriented sol-gel Ce-doped ZnO thin films properties, J. Lumin. 188 (2017) 331–336.
[21] A. Chelouche, T. Touam, M. Tazerout, F. Boudjouan, D. Djouadi, A. Doghmane, Low cerium doping investigation on structural and photoluminescence properties of sol-gel ZnO thin films, J. Lumin. 181 (2017) 448–454.
[22] D. Gao, L. Lyu, B. Lyu, J. Ma, L. Yang, J. Zhang, Multifunctional cotton fabric loaded with Ce doped ZnO nanorods, Mater. Res. Bull. 89 (2017) 102–107.
[23] M. Yilmaz, Z. Caldiran, A. Deniz, S. Aydogan, R. Gunturkun, A. Turut, Preparation and characterization of sol–gel-derived n-ZnO thin film for Schottky diode application, Appl. Phys. A 119 (2) (2015) 547–552.
[24] M. Yilmaz, Ş. Aydoğan, The effect of Mn incorporation on the structural, morphological, optical, and electrical features of nanocrystalline ZnO thin films prepared by chemical spray pyrolysis technique, Metall. Mater. Trans. A 46 (6) (2015) 2726–2735.
[25] Ş. Aydoğan, M. L. Grilli, M. Yilmaz, Z. Çaldiran, H. Kaçuş, A facile growth of spray based ZnO films and device performance investigation for Schottky diodes: determination of interface state density distribution, J. Alloy Compd. 708 (2017) 55–66.
[26] M. Yilmaz, A function of external doping: Characteristics of inorganic nanostructure based diode, Ceram. Int. 45 (1) (2019) 665–673.
[27] A. Özmen, S. Aydogan, M. Yilmaz, Fabrication of spray derived nanostructured n-ZnO/p-Si heterojunction diode and investigation of its response to dark and light, Ceram. Int.
[28] W. I. Park, D. H. Kim, S. Jung, G. Yi, Metalorganic vapor-phase epitaxial growth of vertically well-aligned ZnO nanorods, Appl. Phys. Lett. 80 (22) (2002) 4232–4234.
[29] B. Yao, Y. Chan, N. Wang, Formation of ZnO nanostructures by a simple way of thermal evaporation, Appl. Phys. Lett. 81 (4) (2002) 757–759.
[30] D. Zhang, Z. Xue, Q. Wang, The mechanisms of blue emission from ZnO films deposited on glass substrate by rf magnetron sputtering, J. Phys. D Appl. Phys. 35 (21) (2002) 2837–2840.
[31] J. H. Choi, H. Tabata, T. Kawai, Initial preferred growth in zinc oxide thin films on Si and amorphous substrates by a pulsed laser deposition, J. Cryst. Growth 226 (4) (2001) 493–500.
[32] M. Ambia, M. Islam, M. O. Hakim, The effects of deposition variables on the spray pyrolysis of ZnO thin film, J. Mater. Sci. 29 (24) (1994) 6575–6580.
[33] N. Saito, H. Haneda, T. Sekiguchi, N. Ohashi, I. Sakaguchi, K. Koumoto, Low-temperature fabrication of light-emitting zinc oxide micropatterns using self-assembled monolayers, Adv. Mater. 14 (6) (2002) 418–421.
[34] M. Ahmed, B. S. Mwankemwa, E. Carleschi, B. Doyle, W. E. Meyer, J. M. Nel, Effect of Sm doping ZnO nanorods on structural optical and electrical properties of Schottky diodes prepared by chemical bath deposition, Mater. Sci.Semicond. Process. 79 (2018) 53–60.
[35] M. Ahmed, W. E. Meyer, J. M. Nel, Structural, optical and electrical properties of a schottky diode fabricated on Ce doped ZnO nanorods grown using a two step chemical bath deposition, Mater. Sci. Semicond. Process. 87 (2018) 187–194.
[36] M. Ahmed, W. Meyer, J. Nel, Structural, optical and electrical properties of the fabricated schottky diodes based on ZnO, Ce and Sm doped ZnO films prepared via wet chemical technique, Mater.Res. Bull. 115 (2019) 12–18.
[37] A. Kocyigit, M. Yılmaz, Ş. Aydoğan, Ü. İncekara, The effect of measurements and layer coating homogeneity of AB on the Al/AB/p-Si devices, J. Alloy Compd. 790 (2019) 388–396.
[38] K. Badreddine, I. Kazah, M. Rekaby, R. Awad, Structural, Morphological, Optical, and Room Temperature Magnetic Characterization on Pure and Sm-Doped ZnO Nanoparticles, J. Nanomater. 2018.
[39] N. S. Ramgir, D. J. Late, A. B. Bhise, M. A. More, I. S. Mulla, D. S. Joag, K. Vijayamohanan, ZnO multipods, submicron wires, and spherical structures and their unique field emission behavior, J. Phys. Chem. B 110 (37) (2006) 18236–18242.
[40] J. Zheng, Q. Jiang, J. Lian, Synthesis and optical properties of flower-like ZnO nanorods by thermal evaporation method, Appl. Surf. Sci. 257 (11) (2011) 5083–5087.
[41] Y. Wang, L. Sun, L. Kong, J. Kang, X. Zhang, R. Han, Room-temperature ferromagnetism in Co-doped ZnO bulk induced by hydrogenation, J. Alloy Compd. 423 (1-2) (2006) 256–259.
[42] R. Al-Gaashani, S. Radiman, A. Daud, N. Tabet, Y. Al-Douri, XPS and optical studies of different morphologies of ZnO nanostructures prepared by microwave methods, Ceram. Int. 39 (3) (2013) 2283–2292.
[43] M. Islam, T. Ghosh, K. Chopra, H. Acharya, XPS and X-ray diffraction studies of aluminum-doped zinc oxide transparent conducting films, Thin Solid Films 280 (1-2) (1996) 20–25.
[44] K. D. Kumar, V. Ganesh, M. Shkir, S. AlFaify, S. Valanarasu, Effect of different solvents on the key structural, optical and electronic properties of sol–gel dip coated AZO nanostructured thin films for optoelectronic applications, J. Mater. Scie. Mater. Electron. 29 (2) (2018) 887–897.
[45] J. Yang, M. Gao, L. Yang, Y. Zhang, J. Lang, D. Wang, Y. Wang, H. Liu, H. Fan, Low-temperature growth and optical properties of Ce-doped ZnO nanorods, Appl. Surf. Scie. 255 (5) (2008) 2646–2650.
[46] V. Anand, A. Sakthivelu, K. D. A. Kumar, S. Valanarasu, V. Ganesh, M. Shkir, A. Kathalingam, S. AlFaify, Novel rare earth Gd and Al co-doped ZnO thin films prepared by nebulizer spray method for optoelectronic applications, Superlattices Microstruct. 123 (2018) 311–322.
[47] V. Anand, A. Sakthivelu, K. D. Kumar, S. Valanarasu, A. Kathalingam, V. Ganesh, M. Shkir, S. AlFaify, I. Yahia, Rare earth Sm^{3+} co-doped AZO thin films for opto-electronic application prepared by spray pyrolysis, Ceram. Int. 44 (6) (2018) 6730–6738.
[48] Y. Huang, M. Liu, Z. Li, Y. Zeng, S. Liu, Raman spectroscopy study of ZnO-based ceramic films fabricated by novel sol–gel process, Mater. Sci. Eng.: B 97 (2) (2003) 111–116.
[49] L. Tong, T. Cheng, H. Han, J. Hu, X. He, Y. Tong, M. Schneider, Photoluminescence studies on structural defects and room temperature ferromagnetism in Ni and Ni–H doped ZnO nanoparticles, J. Appl. Phys. 108 (2) (2010) 023906.

[50] V. Kumar, H. Swart, O. Ntwaeaborwa, R. Kroon, J. Terblans, S. Shaat, A. Yousif, M. Duvenhage, Origin of the red emission in zinc oxide nanophosphors, Mater. Lett. 101 (2013) 57–60.
[51] S. Awan, S. Hasanain, G. Hassnain Jaffari, D. H. Anjum, U. S. Qurashi, Defects induced luminescence and tuning of bandgap energy narrowing in ZnO nanoparticles doped with Li ions, J. Appl. Phys. 116 (8) (2014) 083510.
[52] V. Kumar, J. Prakash, J. P. Singh, K. H. Chae, C. Swart, O. Ntwaeaborwa, H. Swart, V. Dutta, Role of silver doping on the defects related photoluminescence and antibacterial behaviour of zinc oxide nanoparticles, Colloids Surf. B Biointerfaces 159 (2017) 191–199.
[53] A. Djurišić, C. Choy, A. L. Roy, Y. H. Leung, C. Kwong, K. W. Cheah, T. Gundu Rao, W. K. Chan, H. Fei Lui, C. Surya, Photoluminescence and electron paramagnetic resonance of ZnO tetrapod structures, Adv. Funct. Mater. 14 (9) (2004) 856–864.
[54] T. Bora, P. Sathe, K. Laxman, S. Dobretsov, J. Dutta, Defect engineered visible light active ZnO nanorods for photocatalytic treatment of water, Catal. Today 284 (2017) 11–18.
[55] K. Vanheusden, C. Seager, W. t. Warren, D. Tallant, J. Voigt, Correlation between photoluminescence and oxygen vacancies in ZnO phosphors, Appl. Phys. Lett. 68 (3) (1996) 403–405.
[56] Y. Heo, D. Norton, S. Pearton, Origin of green luminescence in ZnO thin film grown by molecular-beam epitaxy, J. Appl. Phys. 98 (7) (2005) 073502.
[57] X. Wu, G. Siu, C. Fu, H. Ong, Photoluminescence and cathodoluminescence studies of stoichiometric and oxygen-deficient ZnO films, Appl. Phys. Lett. 78 (16) (2001) 2285–2287.
[58] E. Rhoderick, R. Williams, M. S. Contacts, 2nd edn, Clarendon, Oxford.
[59] L. J. Brillson, Y. Lu, ZnO Schottky barriers and ohmic contacts, J. Appl. Phys. 109 (12) (2011) 8.
[60] N. S. Singh, L. Kumar, A. Kumar, S. Vaisakh, S. D. Singh, K. Sisodiya, S. Srivastava, M. Kansal, S. Rawat, T. A. t. Singh, Fabrication of zinc oxide/polyaniline (ZnO/PANI) heterojunction and its characterisation at room temperature, Mater. Sci. Semicond. Process. 60 (2017) 29–33.
[61] S. M. Sze, K. K. Ng, Physics of semiconductor devices, John wiley & sons, 2006.
[62] Ş. Aydoğan, K. Çınar, H. Asıl, C. Coşkun, A. Türüt, Electrical characterization of Au/n-ZnO Schottky contacts on n-Si, J. Alloy Compd. 476 (1-2) (2009) 913–918.
[63] A. Dey, A. Layek, A. Roychowdhury, M. Das, J. Datta, S. Middya, D. Das, P. P. Ray, Investigation of charge transport properties in less defective nanostructured ZnO based Schottky diode, RSC Adv. 5 (46) (2015) 36560–36567.
[64] L. Brillson, Advances in understanding metal-semiconductor interfaces by surface science techniques, J. Phys. Chem. Solids 44 (8) (1983) 703–733.
[65] N. Mott, Note on the contact between a metal and an insulator or semi-conductor, in: Math. Proc. Camb. Philos. Soc., Vol. 34, Cambridge University Press, 1938, pp. 568–572.
[66] R. L. Anderson, Experiments on ge-gaas heterojunctions, in: Electronic Structure of Semiconductor Heterojunctions, Springer, 1988, pp. 35–48.
[67] A. Jain, P. Kumar, S. Jain, V. Kumar, R. Kaur, R. Mehra, Trap filled limit voltage (V_{TFL}) and V^2 law in space charge limited currents, J. Appl. Phys. 102 (9) (2007) 094505.
[68] M. Zhu, T. Cui, K. Varahramyan, Experimental and theoretical investigation of MEH-ppv based Schottky diodes, Microelectron. Eng. 75 (3) (2004) 269–274.